catalysts

MDPI

Article

Photoelectrocatalytic Degradation of Congo Red Dye with Activated Hydrotalcites and Copper Anode

Sara Argote-Fuentes [1], Rossy Feria-Reyes [2], Esthela Ramos-Ramírez [2,*], Norma Gutiérrez-Ortega [3,*] and Gustavo Cruz-Jiménez [4]

1 Doctoral Program in Water Science and Technology, Engineering Division, Guanajuato Campus, University of Guanajuato, 77 Juarez St, Downtown, Guanajuato GTO 36000, Mexico; sg.argotefuentes@ugto.mx
2 Chemistry Department, Natural and Exact Sciences Division, Guanajuato Campus, University of Guanajuato, w/n Noria Alta, Guanajuato GTO 36000, Mexico; rossyfr@gmail.com
3 Department of Civil and Environmental Engineering, Engineering Division, Guanajuato Campus, University of Guanajuato, 77 Juarez St, Downtown, Guanajuato GTO 36000, Mexico
4 Pharmacy Department, Natural and Exact Sciences Division, Guanajuato Campus, University of Guanajuato, w/n Noria Alta, Guanajuato GTO 36050, Mexico; cruzg@ugto.mx
* Correspondence: ramosre@ugto.mx (E.R.-R.); normagut@ugto.mx (N.G.-O.); Tel.: +52-4737320006 (ext. 1457) (E.R.-R.); +52-4737320006 (ext. 2227) (N.G.-O.)

Abstract: Photoelectrocatalysis is a novel technique that combines heterogeneous photocatalysis with the application of an electric field to the system through electrodes for the degradation of organic contaminants in aqueous systems, mainly of toxic dyes. The efficiency of these combined processes depends on the semiconductor properties of the catalysts, as well as on the anodic capacity of the electrode. In this study, we propose the use of active hydrotalcites in the degradation of Congo red dye through processes assisted by ultraviolet (UV) irradiation and electric current. Our research focused on evaluating the degradation capacity of Congo red by means of photolysis, catalysis, photocatalysis, electrocatalysis, and photoelectrocatalysis, as well as identifying the effect of the properties of the active hydrotalcites in these processes. The results show that a maximum degradation was reached with the photoelectrocatalysis process with active hydrotalcites and a copper anode at 6 h with 95% in a half-life of 0.36 h. The degradation is favored by the attack of the $OH^{\bullet}$ radicals under double bonds in the diazo groups where the electrode produces Cu^{2+} ions, and with the photogenerated electrons, the recombination speed of the electron–hole in the hydrotalcite catalyst is reduced until the complete degradation.

Keywords: photocatalysts; Cu electrodes; diazo dyes; electrocatalysts; layer double hydroxides; photoelectrochemical degradation

Citation: Argote-Fuentes, S.; Feria-Reyes, R.; Ramos-Ramírez, E.; Gutiérrez-Ortega, N.; Cruz-Jiménez, G. Photoelectrocatalytic Degradation of Congo Red Dye with Activated Hydrotalcites and Copper Anode. *Catalysts* **2021**, *11*, 211. https://doi.org/10.3390/catal11020211

Academic Editors: Ioan-Cezar Marcu and Octavian Dumitru Pavel
Received: 1 January 2021
Accepted: 3 February 2021
Published: 5 February 2021

1. Introduction

Wastewater, mainly from the textile industry, contains large amounts of azo dyes, as well as inorganic salts such as NaCl and Na_2SO_4 [1]. These azo dyes are highly toxic, carcinogenic, and mutagenic in nature and can even bioaccumulate in the food chain [2,3]; therefore, we must develop effective methods for the treatment of industrial wastewater that can degrade the synthetic dyes contained in it [4]. Azo dyes are the most consumed in industry, mainly in textiles, representing up to 35% of dye consumption. They are characterized by a structure that contains at least two aromatic compounds linked together by azo type chromophore group (-N=N-) [4]. Various methods, such as adsorption [5], biodegradation [6], chemical oxidation [7], and microbial or enzymatic treatment [8], have been implemented for the elimination of textile dyes from water; however, because these methods are not destructive, a transfer of the contaminant from one phase to another occurs, which requires additional treatments, such as advanced oxidation processes, which, in recent years, have been extensively investigated.

Heterogeneous photocatalysis is considered an emerging destructive technology that leads to the total mineralization of diverse organic contaminants [9–11], in which the degradation of the contaminating compound dissolved in water occurs by the action of semiconductor materials irradiated by light, mainly ultraviolet. Some of the most used photocatalyst metallic semiconductor materials are TiO_2, ZnO, SnO_2, ZrO_2, V_2O_5, WO_3, CeO_2, and g-C_3N_4, as well as several mixtures of these have been studied [12–16]. In the case of TiO_2, despite being the most used photocatalyst, it presents some disadvantages, the main disadvantage is that it presents a relatively high value of the forbidden band energy (approximately, 3.2 eV for the anatase phase and 3.0 eV for the rutile phase), which limits its absorption in the spectrum of the ultraviolet-visible (UV-VIS) region, while also presenting a high rate of recombination of photogenerated electron/hole (e^-/h^+) pairs, which results in a decrease of its photocatalytic activity. That is why much research is focused on improving the application of TiO_2, with the intent to reduce the band gap due to structural modifications [17,18]. Most studies focused on doping TiO_2 with metallic ions such as nickel, manganese, cobalt, titanium, chrome, iron, vanadium, zinc, and copper, as well as with nonmetallic elements or even through the formation of composites with MnO_2, In_2O_3, CeO_2, and MoS_2 [19–21]. There is another alternative currently being studied to improve the photocatalytic activity of TiO_2 in photoactivation using an electric current, which suggests that if a better photoactivation of TiO_2 corresponds to a higher degeneration rate of reactive species, it would also correspond to a higher overall degradation performance [22,23].

Within the alternative material options to TiO_2 are the layered double hydroxides or hydrotalcites, which are compounds used as precursors of oxides, which have shown to be a viable option as photocatalytically active materials [24–27]. Hydrotalcites are composed of inorganic layers with a laminar structure and are chemically characterized by the general formula $[M_{1-x}^{2+}M_x^{3+}\ (OH)_2]x+(A^{n-})_{x/n} \cdot mH_2O$, where M^{2+} (M^{2+} = Mg^{2+}, Ni^{2+}, Co^{2+}, Cu^{2+}, Zn^{2+}) is a divalent cation and M^{3+} (M^{3+} = Al^{3+}, Fe^{3+}, Cr^{3+}, etc.) is a trivalent cation, where both cations' octahedral networks with positive residual charge are structured. A^{n-} are anions that lodge in the interlaminar space to compensate the residual charge of the sheets (A^{n-} = NO_3^-, CO_3^{2-}, SO_4^{2-}, Cl^-, Br^-, I^-, etc.) and m is the amount of water molecules [28,29]. These materials can be easily and economically synthesized at laboratory level. Figure 1 shows the laminar structure of a hydrotalcite Mg/Al with carbonate ions and water molecules in the interlaminar space.

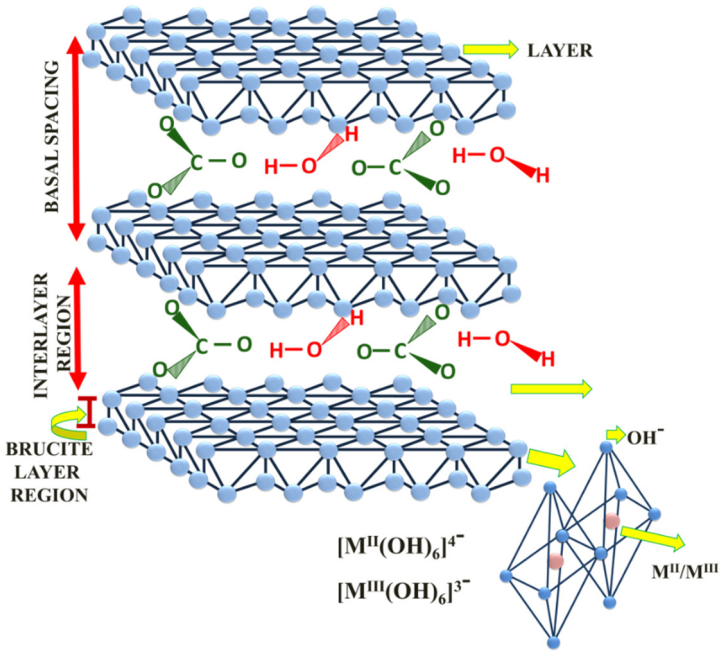

Figure 1. The laminar structure of Mg/Al-CO_3^{2-} hydrotalcite.

Due to its anion exchange capacity in the interlaminar space, hydrotalcites have been used to remove from water mono-, di-, and polyvalent anions, organochlorine compounds [30,31], heavy metals [32,33], and synthetic dyes [5,34–36]. In addition, the chemical composition of hydrotalcites, as well as their physicochemical properties, have allowed their application in various areas such as catalysis [37], electrocatalysis [38,39], energy storage [40,41], and photocatalysis [5,29,31].

Photoelectrocatalysis or photoelectrochemical degradation is a novel form of electrochemistry that combines the techniques of heterogeneous photocatalysis with electrochemical oxidation techniques for the improved removal of organic contaminants in aqueous systems. Its general, rationale is that metal oxides act as semiconductors, and like that in conventional photocatalysis, they produce pairs of electrons–holes that are photogenerated when the anodic material absorbs photons from light irradiation [42,43]. In this research work, the influence of the structural, textural, and thermal properties of activated hydrotalcites on the degradation capacity of synthetic Congo red dye in aqueous solutions was studied using a combined system of photoelectrocatalytic operating parameters.

2. Results and Discussion

2.1. Characterization of Catalytic Precursors of the Hydrotalcites

The X-ray diffractogram obtained from the synthesized solid with a ratio of Mg/Al = 1, hydrotalcite (HT-1) is shown in Figure 2a. The figure shows that the structure is crystalline, corresponding to a hydrotalcite-type material, by showing characteristic peaks with Miller's indexes (003), (006), (009), (012), (015), (018), (110), and (113) (JCPDS 22 0700 Card), with rhombohedral symmetry. In addition, traces of the crude crystalline phase (**001) (Joint Committee on Powder Diffraction Standards-JCPDS card 7-239) and phases of boehmite or hydrated aluminum oxide compound (*, *120, *022) can be identified (JCPDS card 1-1283). This synthesized solid contains the precursor crystalline phases to be activated by heat treatment at 400 °C.

For the HT-2 sample, corresponding to the hydrotalcite of ratio Mg/Al = 1 calcined at 400 °C, the X-ray diffractogram is shown in Figure 2b. It shows that the synthesized hydrotalcite has structurally evolved when treated thermally at 400 °C, and a mixture of crystalline and amorphous phases can be identified. The crystalline phase of the periclase type has characteristic peaks of MgO (JCPDS 4-0829) with the index (111) at 35.48°, the index (200) at 44.40°, and the index (220) at, approximately, 63.04°, which are wider than those of the initial solid, indicating that it has lost crystallinity due to the thermal treatment. Additionally, a dispersed phase of low crystallinity with an amorphous predominance of the magnesium–aluminum spinel-type $MgAl_2O_4$ (***111, ***311, ***440) (JCPDS magnesium–aluminum spinel 21-1152) is observed, which would imply that the solid starts to rehydrate thanks to its memory effect. The oxides obtained by calcination at 400 °C acquire surface properties necessary for the semiconductor activity in the catalytic photoelectrodegradation of the Congo red dye.

Figure 2c shows the X-ray diffraction pattern of the solid calcined at 400 °C after the photodegradation process of the Congo red dye (HT-RC). The material calcined at 400 °C made up of a mixture of mixed and simple Mg-Al oxides regenerated its original hydrotalcite-type structure due to the capacity of these materials to recover their structure through a process called the memory effect. This memory effect is carried out on the structure of the solid after calcination when these come into contact with solutions containing anions or other dissolved substances, as is the case with the Congo red dye, so that the solid uses the carbonate ions present in the solution to reconstruct the original double-laminar structure. The pattern of the solid after photodegradation is the same as that of the fresh hydrotalcite, even with a higher purity since no segregated phases of $Mg(OH)_2$ or $Al(OH)_3$ are observed, and since no displacement is observed in the angle 2θ at the maximum reflection peak, it is confirmed that the interlaminar space of the solid is not increased by the presence of the Congo red dye.

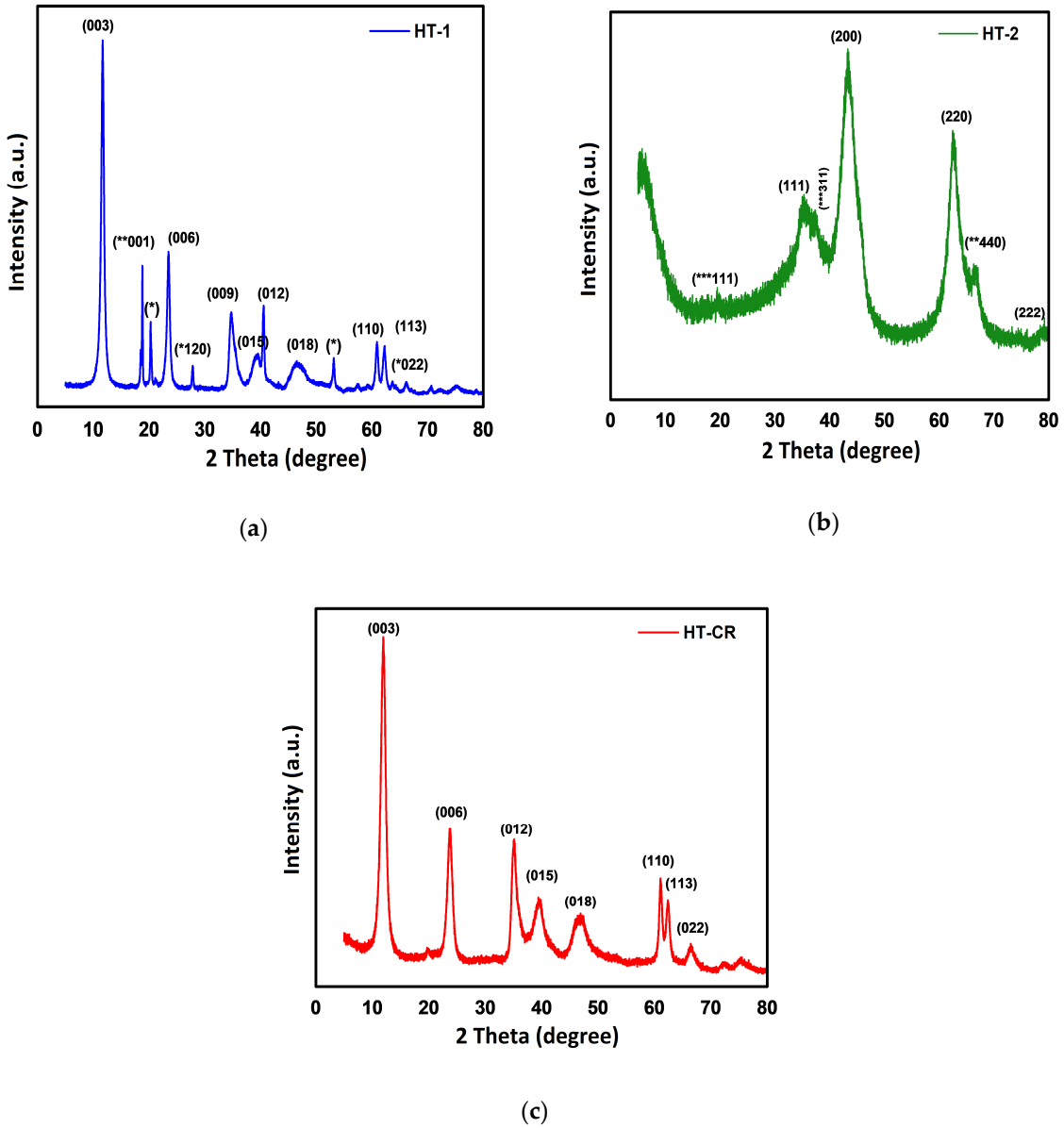

Figure 2. X-ray diffractogram of: (**a**) fresh synthesized hydrotalcite (HT-1) with ratio Mg/Al = 1, (**b**) hydrotalcite calcined at 400 °C HT-2, and (**c**) hydrotalcite after photodegradation of the Congo red.

The thermogravimetric (TGA) and differential thermal (DTA) analysis of the fresh synthesized solid (HT-1) is shown in Figure 3. In this study, the main changes that the synthesized solid exhibits because of the temperature increase associated with the thermal evolution of the solid and its thermal decomposition can be observed. This analysis allows us to identify the appropriate temperature to activate the hydrotalcites to be used as semiconductors in photoelectrodegradation processes. The temperature increases at 198 °C correspond to the first signal of the DTA and are attributed to the endothermic reaction generated by the elimination of the water occluded in the interlaminate of the hydrotalcite's crystalline structure, which represents a loss of 29.7% of the initial mass of the solid in the TGA graph. The second endothermic reaction centered at 355 °C is attributed to the decomposition of the carbonate anions (CO_3^{2-}) eliminated in the form of carbon dioxide and the dehydroxylation reaction of the hydrotalcite sheets that corresponds to the TGA curve in the range of 240–400 °C, presenting a mass loss of 24.5%. The solids are stable up to 500 °C, where finally, their laminar structure collapses and the spinel of the mixed oxide Mg/Al and periclase is formed. The total mass loss was approximately 53%.

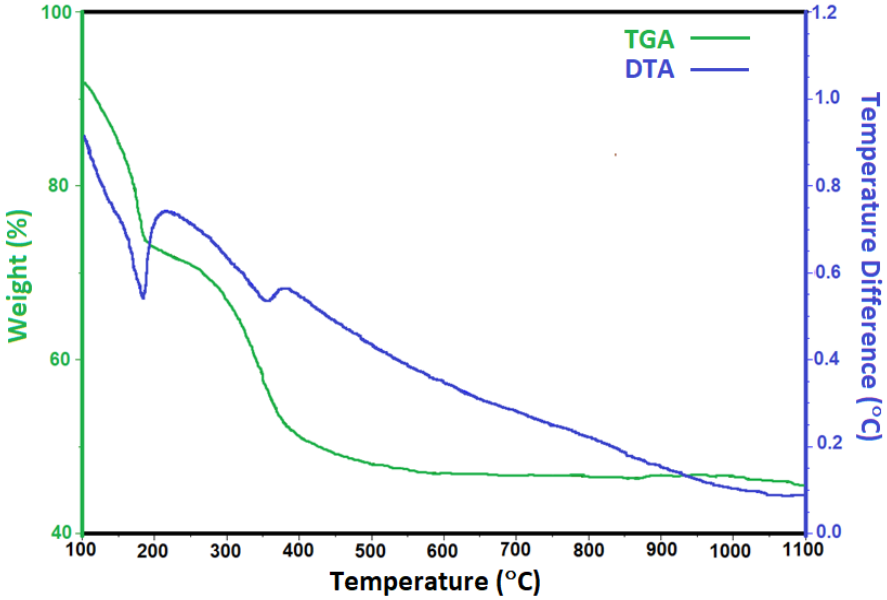

Figure 3. Thermogravimetric analysis (TGA) and differential thermal analysis (DTA) of freshly synthesized hydrotalcite (HT-1).

Figure 4 shows the infrared spectra of the HT-1, HT-2, and HT-RC solids. In all the solids, the characteristic signal of the stretching of the O-H groups of the brucite-type layer with a wide band ranging from 3750 to 3000 cm^{-1} was observed, where for the HT-1 solid, the connection of several signals of greater intensity can be seen, corresponding to the vibration of the OHs of the various crystalline species identified by X-ray diffraction (XRD), as well as the vibration with the interlaminar carbonates and water molecules. This signal becomes less intense and more continuous for the HT-2 solid because the structure has been partially dehydrated. For the HT-RC solid, the intensity increases again due to the reconstruction of the hydrotalcite structure without the presence of other crystalline phases. The signal around 1626 cm^{-1} corresponds to the H-OH vibration of the water molecules, which was observed in the HT-1 solid, disappears in the HT-2 solid that has been calcined, and reappears in the HT-RC solid by the effect of reconstruction of the lamellar structure. Regarding the band present in 1380 cm^{-1}, a fine and intense signal was observed for the HT-1 solid that corresponds to the vibration of the interlaminar CO_3^{2-}, which decreases in intensity for the HT-2 solid due to partial decarbonization with the appearance of a band at 1529 cm^{-1} of the free CO_3^{2-} to be adsorbed on the solid, and finally, in the HT-RC solid, the band intensifies again around 1274 cm^{-1} of the carbonates again in the interlaminar space.

The bands below 1000 cm^{-1} were assigned to the stretching of the metallic oxides Al-O, Mg-O, Al-O-Al, and Al-O-Mg. Specifically, the bands at 669 and 551 cm^{-1} disappear for the HT-2 solid due to the segregation of the crystalline phases of the simple oxides; they are formed again in the HT-RC solid due to the lamellar reconstruction of the hydrotalcite. Additionally, in the HT-RC solid, besides the abovementioned signals of the hydrotalcites, the spectrum is characterized by the presence of a small amount of the Congo red dye adsorbed in the solid, given the signals of the absorption bands at 1725 cm^{-1} that correspond to the presence of double bonds in the diazo groups -N=N, at 1047 cm^{-1} that is attributed to the vibration frequency of the C-N bond, and at 793 cm^{-1}, for the elongation vibration of the SO_3^- group.

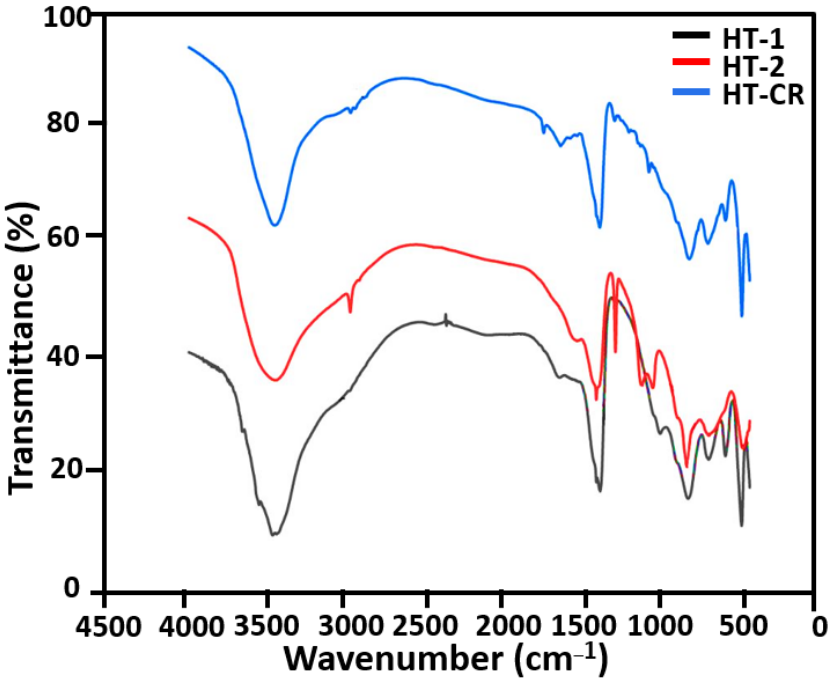

Figure 4. Fourier-transform infrared (FTIR) spectra of HT-1, HT-2, and Congo red dye (HT-CR) samples.

The N_2 adsorption–desorption isotherms of the HT-1 and HT-2 solids are presented in Figure 5. The fresh hydrotalcite HT-1 and the one calcined at 400 °C, HT-2, present type IV isotherms according to the IUPAQ classification with a hysteresis loop of H3 type, which confirms the existence of laminar particle aggregates that, in turn, originate pores in the form of cracks or fissures. This behavior is associated with the presence of mesopores formed by the accommodation of crystalline structures. Regarding the values of the specific area, it is observed that the HT-2 solid has a larger specific area than the HT-1 sample, which is attributed to the thermal decomposition that produces the decarbonation and partial decarboxylation that increases the size and volume of pores.

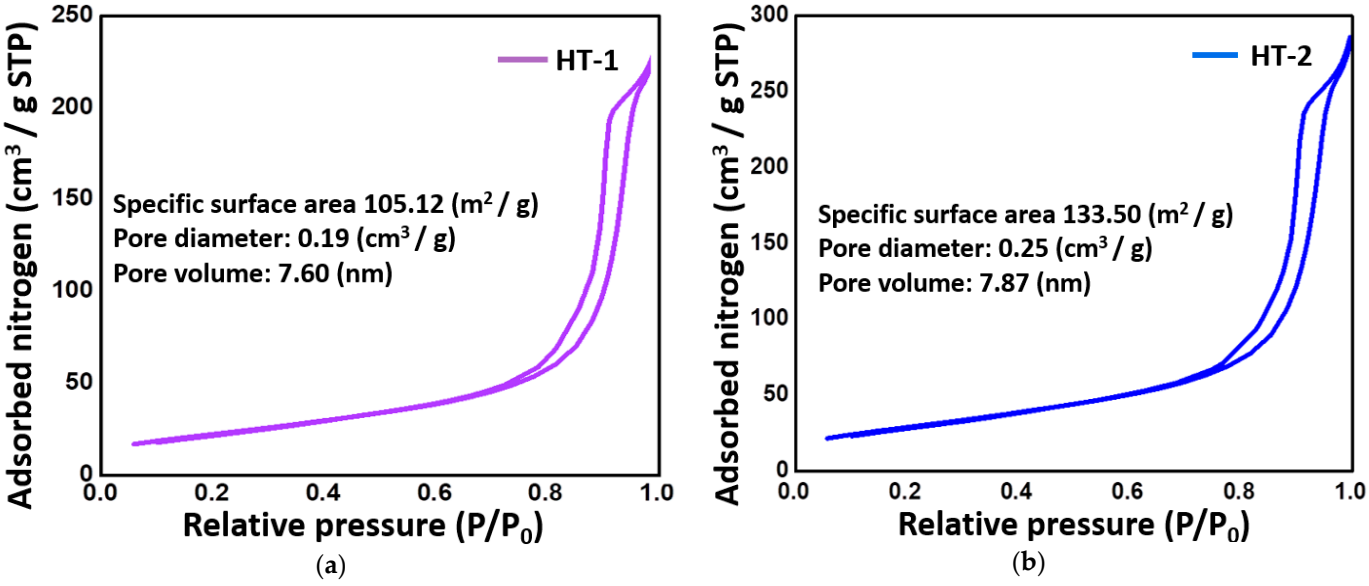

Figure 5. Isotherms of N_2 adsorption-desorption of solids and textural property values: (**a**) HT-1 and (**b**) HT-2.

Figure 6a shows the scanning electron microscopy images of the HT-1 solid corresponding to the synthesized HT-1 hydrotalcite, in which particles formed by lamellar aggregates can be observed as scales. Figure 6b shows the HT-2 solid of calcined hydrotalcite, which also shows particles with crystalline aggregates larger than the fresh solid and with smaller particles attached. Finally, Figure 6c shows the hydrotalcite reconstructed after the photodegradation process where particles formed by thin sheet aggregates like the original structure are observed.

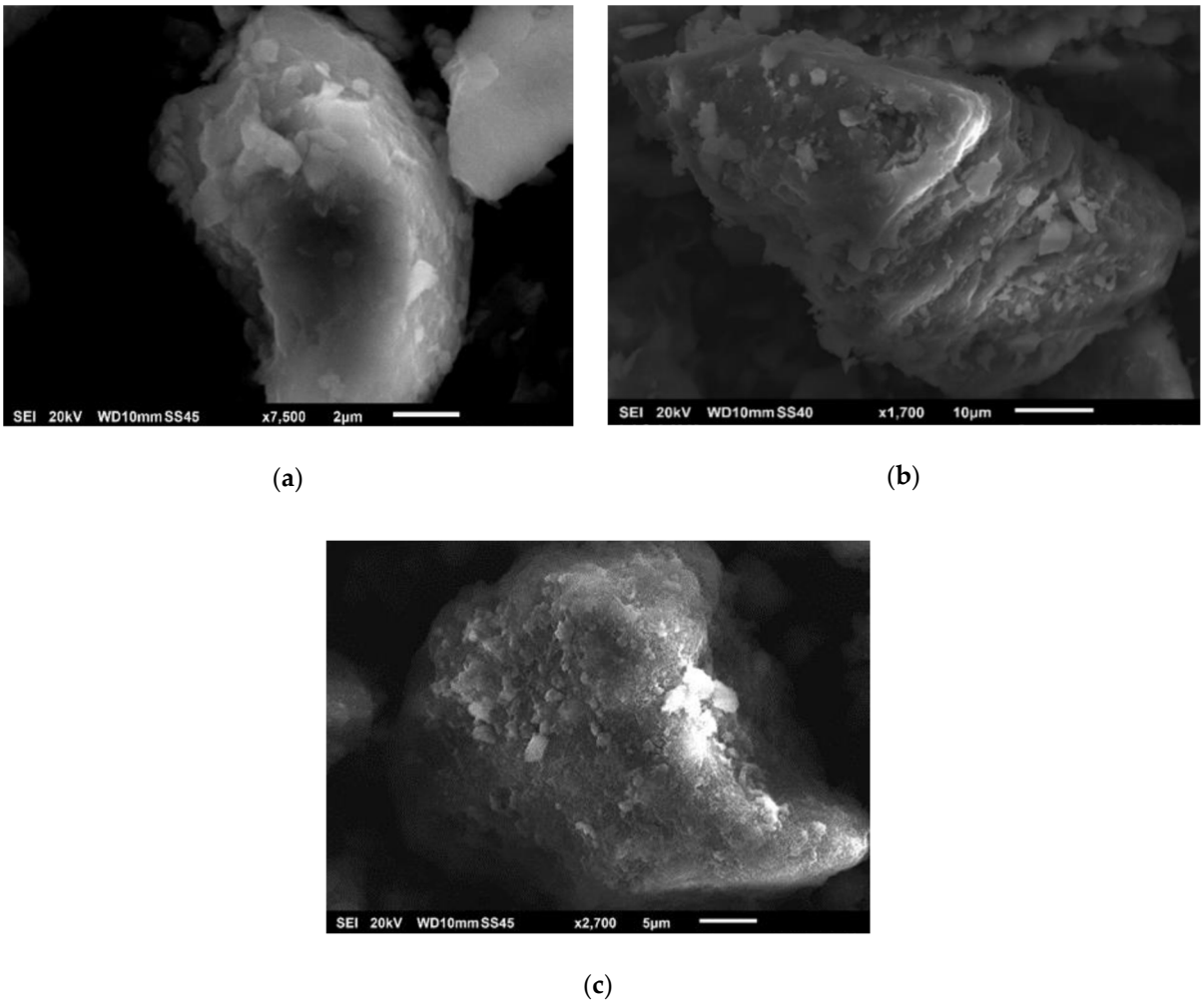

Figure 6. Scanning electron microscopy (SEM) images of: (**a**) fresh synthesized hydrotalcite HT-1 with ratio Mg/Al = 1, (**b**) hydrotalcite calcined at 400 °C HT-2, and (**c**) hydrotalcite after photodegradation of the Congo red.

Figure 7a shows the UV-VIS diffuse reflectance spectrum of the HT-2 photocatalyst used to degrade Congo red. For calculating the optical band gap energy (Eg), Tauc's graphical method was used (Figure 7b). The result for the catalyst treated at 400 °C before photodegradation was 3.28 eV. According to this value, this photocatalyst has a potential application in the degradation of Congo red, so it could favor the photodegradation capacity, considering that it has similar values compared to TiO_2, whose Eg values are reported to be between 3.0 and 3.2 eV [23].

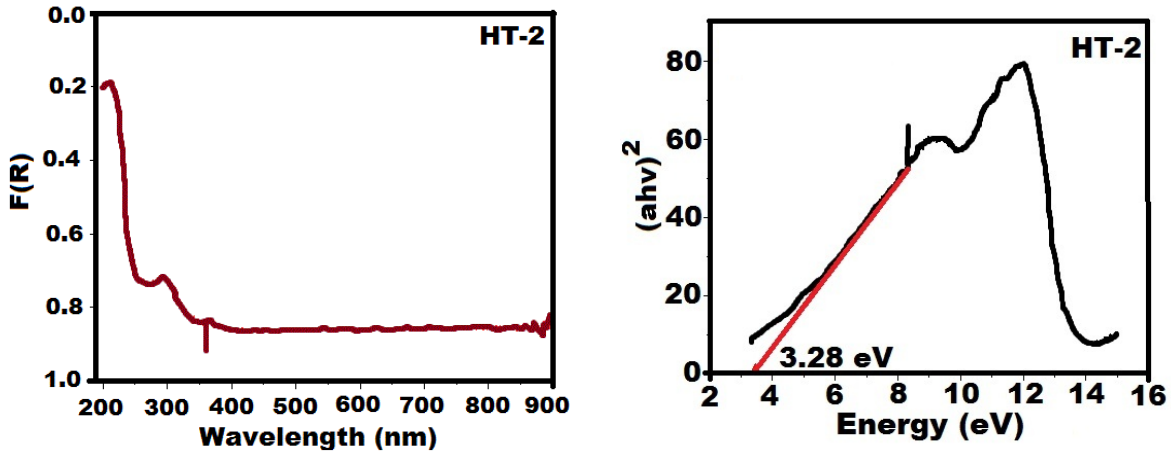

(**a**) (**b**)

Figure 7. Determination of the energy of the forbidden optical band: (**a**) ultraviolet-visible (UV-VIS) diffuse reflectance spectrum of the HT-2 photocatalyst and (**b**) graph of the calculation of the optical band gap energy (Eg) value by Tauc's method for the catalyst at 400 °C before photodegradation.

2.2. Evaluation of the Degradation Capacity of the Congo Red Dye by Photolysis, Catalysis, Photocatalysis, Electrocatalysis, and Photoelectrocatalysis

The standardization of the analytical method for the quantification method of the dye was done using high-performance liquid chromatography (HPLC). The calibration curve for the industrial-grade synthetic dye Congo red in a concentration range of 0.5–40 mg/L, as shown in Figure S1, showed a linear correlation of 0.9991, which allowed us to validate the method for use. With the HPLC-optimized method, samples of each of the degradation processes of the Congo red dye were analyzed.

Figure 8 shows the degradation kinetics of a Congo red dye solution from an initial concentration of 400 mg/L using different systems: photolysis, catalysis, photocatalysis, electrocatalysis, and photoelectrocatalysis in a maximum time of 6 h. The aim of the study was to identify the effect of each of the elements involved in the system of photoelectrocatalysis and its degree of participation in the catalytic activity of 200 mg of catalyst. In the figure, we can see that the effect of photolysis results in a gradual decrease in the concentration of the dye by 8.75% at 4.5 h, remaining constant after that time. In the case of catalysis, that result implies the contact of the catalyst with the dye producing a decrease in the concentration until reaching 46% at 5.5 h. In photocatalysis, the effect of light on the catalyst accelerates the speed of degradation, reaching, in the first hour, more than 50% of the degradation up to 75% at 6 h. Concerning electrocatalysis, the effect of current is greater and more effective on the catalyst, reaching 62% degradation in 1 h and a maximum capacity of 85% at 3.5 h. Finally, the combined effect of UV light irradiation with an electric current on the catalyst reaches a degradation of 87% in 0.5 h, 91% in 1 h, and 96% at 6 h.

With the data from the kinetic studies, the models for each process of degradation of the Congo red dye for the Langmuir–Hinshelwood isotherm for the pseudo-first order were applied as shown in Figure 9a and for the pseudo-second order Ho model as shown in Figure 9b.

Figure 9, coupled with the data in Table 1 shows that only the photolysis and catalysis systems fit the pseudo-first-order kinetic model, which is attributed to the low concentration of hydroxyl radical species formed in the process. In the case of photocatalysis, electrocatalysis, and photoelectrocatalysis processes, it fits better to the pseudo-second-order kinetic model of Ho, which is attributed to the fact that the degradation process requires different stages that imply the formation of different species, mainly the hydroxyl radicals that can be identified by high-resolution liquid chromatography. The pseudo-first-order model assumes that the speed of the degradation reaction is linearly proportional to

the concentration. In contrast, the pseudo-second-order model assumes that the degradation process is controlled by the reactions that occur in the system due to chemisorption in the catalyst, as well as the process of sharing or exchanging electrons between the catalyst, the electrode, and the Congo red. In recent years, degradation processes have been reported that present this type of kinetic behavior, mainly when composites or combined systems are used [44–47].

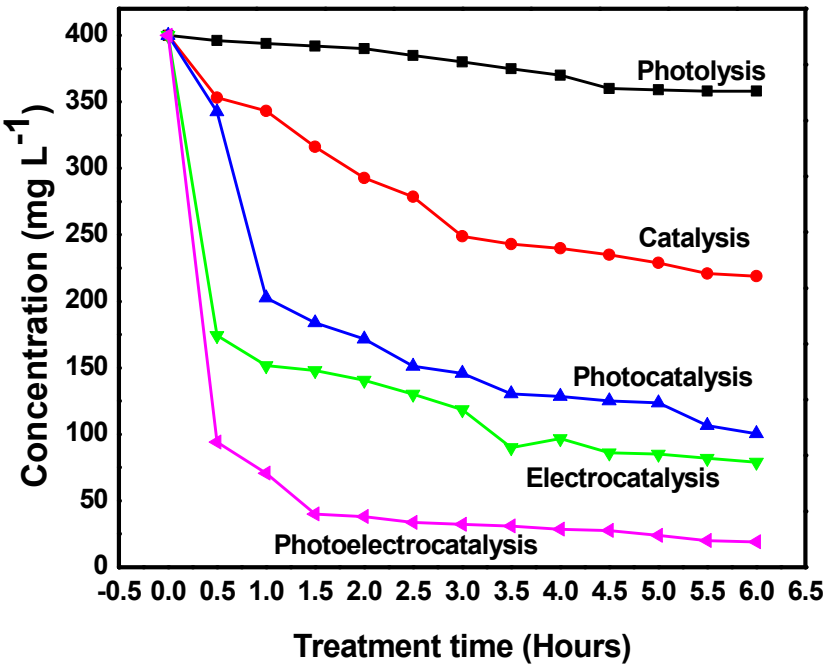

Figure 8. Degradation of Congo red dye by photolysis, catalysis, photocatalysis, electrocatalysis, and photoelectrocatalysis.

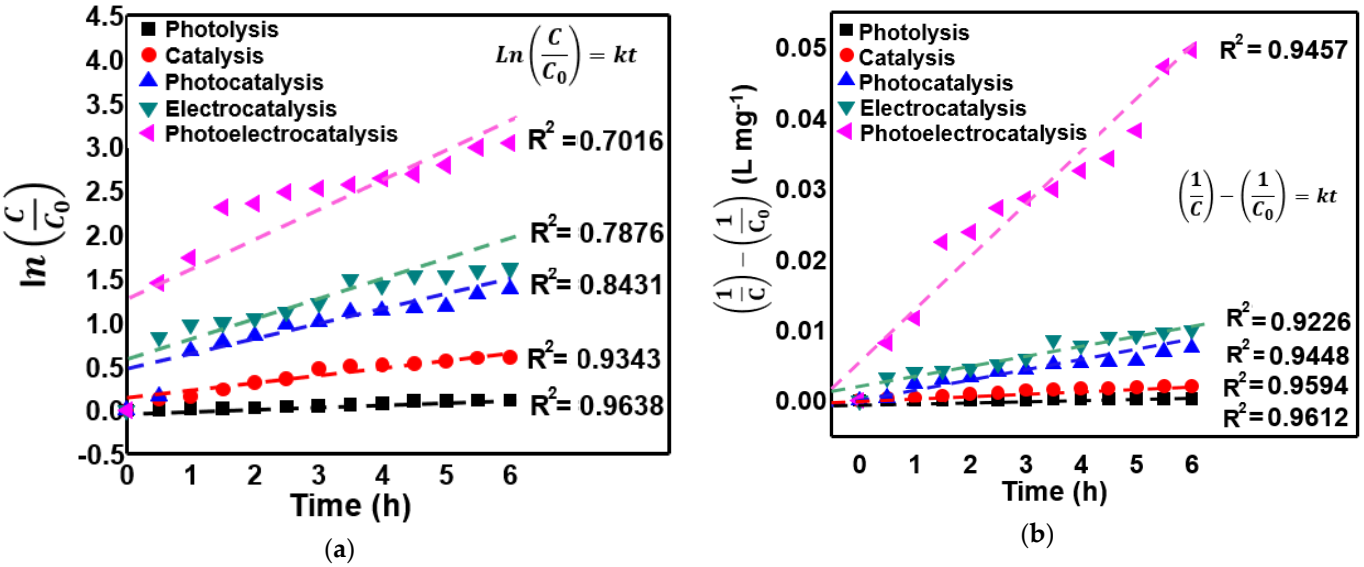

Figure 9. Kinetic models of the different degradation processes of the Congo red dye: (**a**) pseudo-first-order reaction and (**b**) pseudo-second-order reaction.

Table 1. Order of reaction, speed constant, and half-life of the degradation of the Congo red dye for each of the processes.

Process	Pseudo-First Order			Pseudo-Second Order		
	K (h^{-1})	$t_{1/2}$ (h)	R^2	K ($L \cdot mg^{-1} \cdot h^{-1}$)	$t_{1/2}$ (h)	R^2
Photolysis	0.0212	32.69	0.9638	0.00006	41.67	0.9612
Catalysis	0.0990	7.00	0.9343	0.0004	6.25	0.9594
Photocatalysis	0.1975	3.51	0.8421	0.0011	2.27	0.9448
Electrocatalysis	0.2027	3.42	0.7876	0.0015	1.67	0.9226
Photoelectrocatalysis	0.3515	1.97	0.7016	0.0072	0.35	0.9457

Figure 10 shows the chromatograms corresponding to the degradation kinetics of 400 mg/L and the degradation by products of Congo red when using hydrotalcites activated at 400 °C as catalysts. The signal corresponding to the dye appears in an elution time of 1.6 min, and it can be observed that the concentration of the dye gradually decreases with respect to the treatment time in each process analyzed. Thus, in Figure 10a, the chromatograms correspond to the catalysis process of hydrotalcite with the Congo red dye, and at 1.2 min, a signal appears that is attributed to the formation of reactive oxygen species (ROS) such as $^{\bullet}O_2$, $OH^{\bullet}$, H_2O_2, hydroperoxyl ($ROOH^{\bullet}$), and peroxynitrile ($ONOO^{\bullet}$)—these are some of the reactive species formed during the processes studied and that can be detected in concentrations of picomoles, employing chromatography techniques [48–50]. It should be emphasized that the established technique was used only to detect the signal corresponding to the Congo red color and not the reactive oxygen species. Thus, during the catalytic process, we observed that the maximum concentration of the reactive species occurs during the first hour of the process with a value of 1.5×10^{-3} absorbance units (A.U.), and that the generation of the reactive oxygen species decreases with the treatment time; this can be attributed to the fact that the MII/MIII pairs decrease their redox pairs. In Figure 10b, the degradation of the dye is favored by ultraviolet radiation, which causes an increase in reactive species of up to 3.5×10^{-3} A.U. in 4 h of treatment and in which it can be observed that no secondary products are generated during its degradation process. In this case, the degradation is greater because the hydrotalcite is photoactivated by the presence of ultraviolet light, where the photoactivity is related to the forbidden band energy of the crystalline phases and its textural properties [51,52].

For the degradation process using the photocatalyst of hydrotalcite calcined at 400 °C confirmed mainly by the amorphous spine phase $MgAl_2O_4$ and the crystalline periclase phase, it can be considered that the catalyst absorbs a photon, which causes an electron to be transferred from the valence band to the conduction band, leaving a hole in the valence band [53], as shown in Equation (1).

$$MgAl_2O_4 + MgO + h\nu \rightarrow h^+{}_{VB} + e^-{}_{CB} + MgAl_2O_4 + MgO \quad (1)$$

This contributes to the dissociation of water molecules and to the formation of free radicals due to the presence of ultraviolet light, according to Equations (2)–(6) [51].

$$H_2O \longleftrightarrow H^+ + OH^- \quad (2)$$

$$h^+{}_{VB} + H_2O \rightarrow H^+ + {}^{\bullet}OH \quad (3)$$

$$e^-{}_{CB} + O_2 \rightarrow O^{\bullet -}{}_2 \quad (4)$$

$$O^{\bullet -}{}_2 + 2H_2O \rightarrow 2{}^{\bullet}OH + 2OH^- + O_2 \quad (5)$$

$$O^{\bullet -}{}_2/{}^{\bullet}OH + \text{organic compounds} \rightarrow \text{degradation} \quad (6)$$

For the electrocatalysis process in Figure 10c, the application of the electric field increases the generation of the reactive oxygen species from 2.0×10^{-3} to 4.0×10^{-3} A.U.

in 3 h of treatment. This is because the Cu^0/Cu^{2+} ions that are generated on the surface of the electrode and the free electrons of the MII/MIII pair of hydrotalcites that accelerate the degradation of the dye due to the application of the electric field are present in the aqueous medium. In the photoelectrocatalytic process shown in Figure 10d, the reactive oxygen species reach a value of 6.0×10^{-3} A.U. in the first hour of treatment due to the simultaneous application of the electric field and the ultraviolet radiation, which favors the formation of a higher concentration of •OH radicals in the cathode and accelerates the degradation of the Congo red dye. The electrolysis reactions in the aqueous medium are described in Equations (7)–(9) and occur simultaneously with Equations (1)–(6) described above due to the application of the electric field [54]:

$$\text{Anode } H_2O \rightarrow 2H^+ + \frac{1}{2} O_{2(g)} + 2e^- \quad (7)$$

$$\text{Cathode } 2H_2O + 2e^- \rightarrow 2OH^- + H_{2(g)} \quad (8)$$

The above reaction, coupled with the reaction of copper oxidation in an aqueous medium by the application of an electrical potential, produces the reaction shown in Equation (9).

$$Cu^0 \rightarrow Cu^{2+} + 2e^- \quad (9)$$

Under these conditions in the photochemical reactor and in the presence of ultraviolet light, copper used in a wide range of accessible oxidation states, such as Cu0, Cu^+, Cu^{2+}, and Cu^{2+}, generated by the electrolysis reaction could react with the photographed electrons according to the reaction shown in Equation (10) [55].

$$Cu^{2+} + e^-_{CB} \rightarrow Cu^+ \quad (10)$$

In the presence of an electric field, the OH^- and Cu^{2+} ions are generated on the surface of the cathode and the anode simultaneously, and the Cu^{2+} and OH^- ions react in the solution to produce CuO and CuO_2.

$$2Cu^+ + 2OH^- \rightarrow CuO + Cu_2O \quad (11)$$

$$Cu^+ + (O_2, H_2O_2, O_2, \text{other oxidants}) \rightarrow Cu^{2+} + e^- \quad (12)$$

In the case of photoelectrocatalysis, the presence of the catalyst formed by the structure of the activated hydrotalcites (HT-2) containing Mg^{2+} and Al^{3+} favors an increase in the catalytic activity by slowing down the recombination of the electron–hole pairs for the reaction system shown in Equation (9), which considers the formation of Cu^{2+} ions and the generation of e^-. The electrons in the valence band of the activated hydrotalcite are transferred directly to copper, which produces oxidation to Cu^{2+} and Cu^+ species, and the voids created in the hydrotalcite valence band contribute to the degradation of the organic compounds. Figure 11 graphically depicts the potentials for interfacial load transfer and the potentials for recombination of each of the reactive species present in the heterogeneous photoelectrocatalytic system.

The excess of electrons contributed by the copper electrode and the recombination of the same one on the hollow electron pairs of the hydrotalcites accelerate the supply of electrons so that the degradation of the red dye occurs in the photoelectrocatalytic system. For this degradation process to occur, the number of electrons involved in the total combustion of the Congo red dye was set at 178, assuming that the main process is the formation of nitrate and sulfate ions, as shown in Equation (13) [12,56–58].

$$C_{32}H_{22}S_{22}\text{-} + 84H_2O \rightarrow 32CO_2 + 6NO_3{}^- + 2SO_4{}^{2-} + 19H^+ + 178e^- \quad (13)$$

The Cu^{2+} and Cu^+ ions with the photogenerated electrons decrease the recombination speed of the electron–hole pair, generating a higher catalytic activity in the degradation of the Congo red dye, which visually produces the loss of color. For the photoelectrocatalysis

process with which different active chemical species for the degradation are generated, the elimination of 95% of the Congo red dye is achieved.

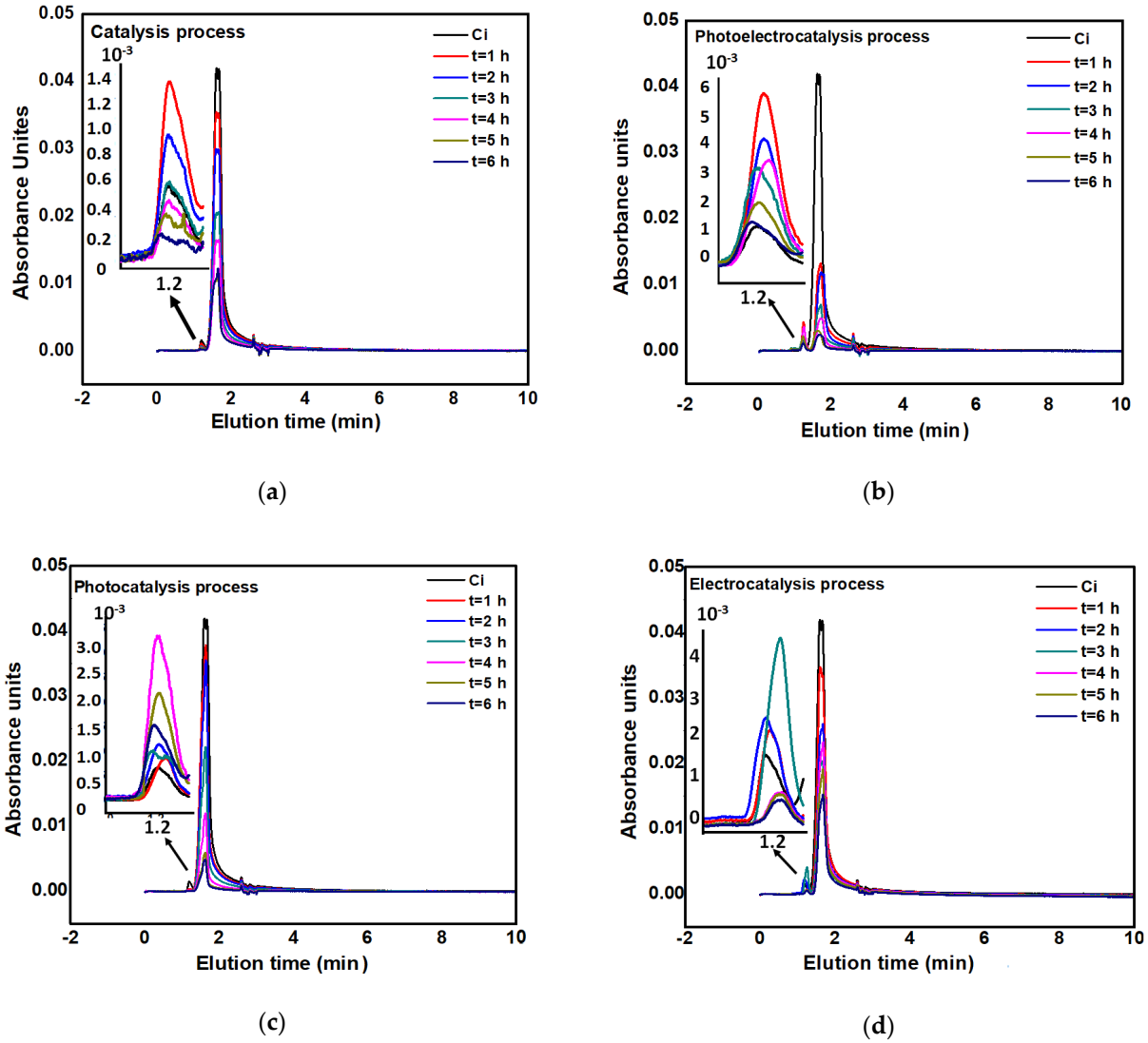

Figure 10. Chromatograms of the degradation of 400 mg/L Congo red by the different processes of degradation: (**a**) catalysis, (**b**) photocatalysis, (**c**) electrocatalysis, and (**d**) photoelectrocatalysis. Isocratic flow 1.0 mL/min = 480 nm using a Thermo chromatographic column Scientific™ Hypersil™ BDS C18 reverse-phase (250 mm × 4.6 mm) and 5 µm particle size. pH 6.7; methanol/water mobile phase 60:40 (*v*/*v*).

Degradation products formed at the end of each process were analyzed by liquid chromatography–mass spectrometry (LC–MS) and identified by interpreting their mass spectra data presenting their molecule ion peaks with respect to m/z (where m is the molecular weight of the intermediates in the mass spectra). The main species detected in the solutions are presented in Figure S2, including LC–MS spectra for the aqueous solution of 10.0 mg/L Congo red.

Figure S2a shows the chromatogram of the 10 mgL^{-1} standards of Congo red. Congo red is a sulfonated compound with two sulfonic acid groups, and degradation can occur in various stages by an electrophilic attack on the benzene rings or a rupture of the bond -C-S- between the aromatic ring and the sulfonate groups. In each one of the chromatograms of the different processes, the intermediate products can be identified; at 633 and 550 m/z, two pseudomolecular ions are identified, where the 633 m/z ions were due to the "M − 2Na + H" [59]. The elimination of the two sulfonate groups and a benzene ring generates

an intermediate with 468.8 and 386.8 m/z; the intermediate by direct fragmentation is 2-nitrosonaphthalene (m/z = 157). The additional oxidation by OH^- radicals is produced by the presence of 3-carboxy propanoate (m/z = 117), 4-carboxybutanoate (m/z = 131), acetic acid (m/z = 60), achieving, in this way, the degradation of the red Congo in the medium. According to the results, the Congo red degradation route as indicated in Figure S2f was used, showing the species detected for the Congo red aqueous solution, and showing possible species formed after the irradiation of the Congo red/HT-2 solution.

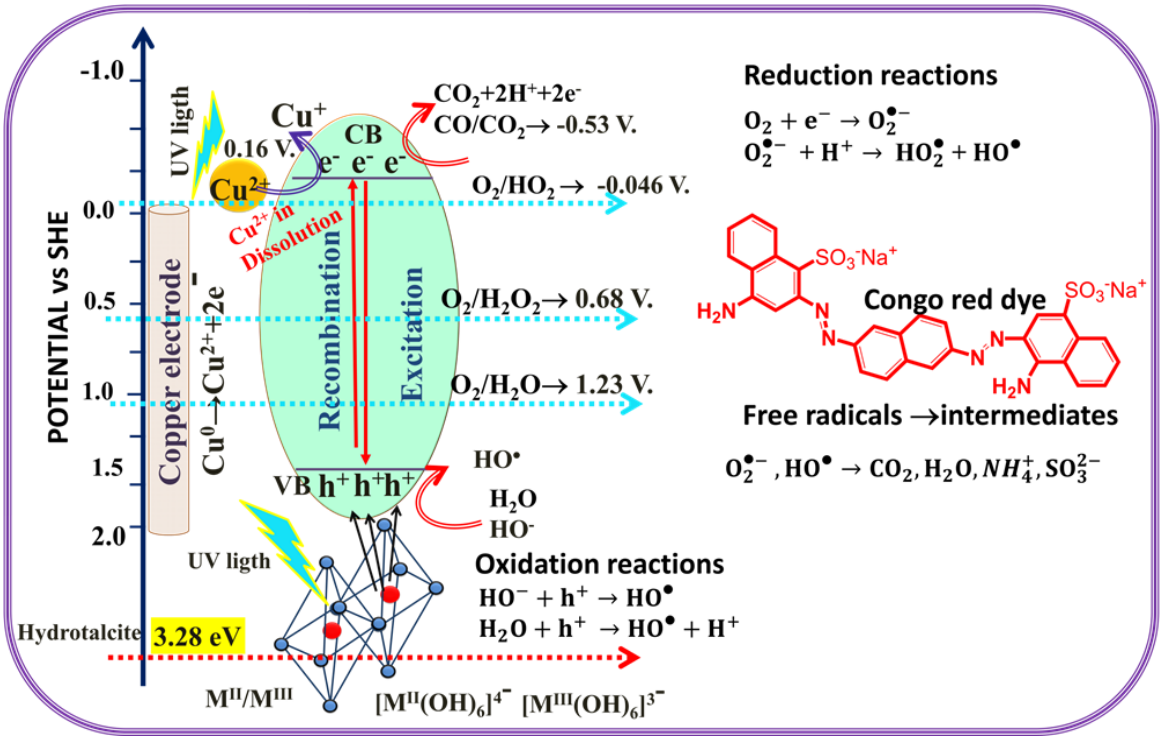

Figure 11. The mechanism for generating photoelectrocatalytic activity of Cu(II)/HT-2 under ultraviolet (UV) light irradiation. The UV light irradiation induces interfacial charge transfer (IFCT) from the hydrotalcite (HT) valence band (VB) to the Cu^{2+} ion. [47]. Copyright American Chemical Society, 2009.

The degradation of the Congo red molecule is favored due to the presence of double bonds in the diazo groups (-N=N-), which is the preferred site for the attack of the •OH radicals. Such an attack can occur in the proximal or distal nitrogen atom of the azo group leading to a variety of cleavage pathways resulting in several identifiable products. The complete destruction of the chromophore leads to the discoloration of the solution with subsequent degradation of the rest of the dye's organic structure.

Figure S3 shows how the Congo red dye is significantly degraded by the photocatalytic process, as shown in Figure S3b, and how the degradation of the dye is complete using the photoelectrocatalytic process according to Figure S3c.

Table 2 shows research that has used TiO_2 reference photocatalysts for Congo red degradation, comparing the photocatalyst used, the concentration of the dye, the degradation time, and the source of irradiation.

Table 2. Comparative study of the photodegradation of the Congo red dye with different TiO_2 materials.

Photocatalyst	Congo Red Concentration (mg/L)	Catalyst Concentration (g/L)	Time (h)	Removal (%)	Irradiation Source	Reference
Nanocrystalline TiO_2 Degussa P-25	20	0.25	0.5	98	Suntest 675 Wm^{-2}	[10]
Mg-TiO_2-P25 NPs	7	0.5	7	80	400 nm vis lamp	[60]
TiO-W	30	0.15	0.83	96	365 nm vis lamp	[61]
TiO_2	55	1.0	8	20	254 nm UV lamp	[62]
Photoelectrocatalysis	400	0.66	1	91	254 nm UV lamp	This work

TiO_2 nanoparticles under the same UV irradiation conditions can only degrade a low percentage despite having low concentrations and a higher amount of catalyst. TiO_2 improves its photodegradation capacity but requires combining with other metals and can only reach high removal percentages if the concentration of Congo red is low and/or with long irradiation times. The results of this research suggest that degradation of Congo red dye using combined photoelectrolytic systems with activated hydrotalcites and Cu anode has improved efficiency at high concentrations of Congo red, making it a promising system for application in effective degradation of the contaminant in aqueous systems. Among the main advantages offered by the use of activated catalysts as photo and electrostimulated catalysts in a degradation system, are the ability to generate pairs of electron holes, as well as the possibility of recovering the catalyst for other recycles thanks to the effect memory.

3. Materials and Methods

3.1. Obtaining the Catalytic Precursors of the Hydrotalcites

Hydrotalcites were synthesized by the coprecipitation method from magnesium nitrate hexahydrate [$Mg(NO_3)_2{\cdot}6H_2O$], aluminum nitrate nonahydrate [$Al(NO_3)_3{\cdot}9H_2O$], and sodium carbonate (Na_2CO_3) in a basic medium at pH 11.5, from stoichiometric amounts of Mg/Al = 1. The synthesized hydrotalcite was dried in an oven at 80 °C for 24 h, and then, a portion was calcined in a muffle at 400 °C for 4 h at a heating rate of 10 °C/min. The fresh solid and solid calcined at 400 °C were ground in an agate mortar until a fine particle size was obtained and were labeled as HT-1, to the fresh hydrotalcite, and HT-2, to the hydrotalcite calcined.

3.2. Structural, Thermal, and Textural Characterization of Hydrotalcite-type Catalytic Precursors

For the characterization and identification of the crystalline structures present, an Inel Equinox Powder Diffractometer coupled to a copper anode and using a monochromatic radiation source from CuKα, whose wavelength (λ) was 1.5418 Å, in a range of 5–80 theta degrees with a step size of 0.02° and a scanning speed of 2°/min was used.

The thermal, differential, and thermogravimetric evolution profile (DTA and TGA) was carried out using Thermo-analyzer TA instruments (New Castle, DE, USA), at a heating rate of 10 °C/min in an air atmosphere at a speed of 100 mL/min, and using α-alumina as a reference standard.

For the identification of the functional groups, including the different types of vibration in their links present in the materials that could suggest a structural composition, as well as for the identification of the presence of anions in the interlaminar space, the infrared spectra with Fourier transforms (FTIR) were obtained using a Perkin Elmer Spectrum 100 FT-IR Spectrometer equipment in (Waltham, MA, USA) a wavelength range between 500 and 4500 cm^{-1}; the samples were prepared by mixing the solid with KBr (the target) in a 1:100 ratio.

The textural characterization was carried out using the technique of nitrogen (N_2) physisorption in an automated Micromeritics TriStar ll Plus equipment. Before being analyzed, the samples were degassed by heating to 110 °C for 3 h in an atmosphere of helium, and then, they were left to cool down to room temperature; the distribution of

the size of the pore was calculated based on the curves of desorption of the isotherms of Barrett–Joyner–Halenda (BJH). Using the Brunauer, Emmett, and Teller (BET) theory, the textural properties of the solids, such as specific area, pore size, and pore diameter, were determined, as well as the nitrogen adsorption–desorption isotherms.

The morphology was analyzed in a JSM 6010/ LV field-emission scanning electron microscope at an acceleration voltage of 20 Kv.

The determination of the band gap energy of the catalyst was carried out by the diffuse reflectance technique in a Shimadzu UV-Vis model 2401-PC equipment with integration sphere.

3.3. Optimization of the Analytical Method for the Quantification of the Degradation of the Congo Red Dye

A chromatography analysis of each of the processes was made in triplicate and aliquots of 2 mL were taken every 30 min and centrifuged at 14,000 rpm for 15 min. The samples were then passed through 0.2 μm Iso-Disc™ filters N-25-2, Nylon 25 μm × 0.2 μm Supelco, to separate the suspended particles from the supernatant. From the previously filtered solutions, 100 μL of the samples are taken and diluted with 900 μL milli-Q water. For the detection of high-resolution liquid chromatography, 20 μL of the solution was injected through a Thermo Chromatographic Column Scientific™ Hypersil™ BDS C18 reverse-phase (250 mm × 4.6 mm and particle size of 5 μm) at a wavelength of 480 nm, 2150 psi, and 26 °C using a Perkin Elmer 1000 chromatograph with a diode array detector. Analysis of degradation products of Congo red was done by liquid chromatography–mass spectrometry (LC–MS) measurements were performed using Agilent 1100 series (Waldbronn, BW, Germany) with electrospray ionization mass spectrometry. All the reagents used for the analysis were of analytical grade; acetonitrile (J.T. Baker 99%) and methanol (J.T. Baker 99%), and water was from Milli-Q of 18.0 μS.

3.4. Evaluation of the Degradation Capacity of Congo Red Dye by Photolysis, Catalysis, Photocatalysis, Electrocatalysis, and Photoelectrocatalysis

All these degradation tests of the Congo red dye were performed in triplicate using a photochemical reactor RFQ-500 in a closed system with constant agitation and room temperature, taking aliquots of 2.0 mL every 30 min during the experiment. For the catalytic degradation tests, 300 mL of Congo red dye solution at a concentration of 400 mg/L were used in contact with 200 mg of HT-2 catalyst (hydrotalcite calcined at 400 °C). For the photocatalytic degradation tests, a 120 V, 9-watt UV lamp of radiation of 254 nm was used. The initial reaction temperature was 25 °C with a maximum of 29 °C in all tests. In the electrocatalysis and photoelectrocatalysis tests, a potentiostat (BioLogic Science Instrument, EC-Lab Version 10.12 software, France) was used, and a potential of 25.0 millivolts was applied through a copper electrode with an area of 3.0 cm^2 as the anode and L302 stainless steel as the cathode, as shown in Figure S4.

4. Conclusions

In this study, Mg/Al hydrotalcite type materials were prepared by the coprecipitation method to be used as heterogeneous catalysts in the degradation of Congo red dye under different degradation systems. The hydrotalcite type catalysts activated at 400 °C showed a combination of crystalline and amorphous phases of $MgAl_2O_4$ and MgO that show semiconductor surface properties associated with a forbidden band energy of 3.28 eV, confirming particles with slit type mesopores with specific areas above 133 m^2/g that provide them with favorable textural properties for dye access for its degradation assisted by ultraviolet (UV) irradiation and/or electric current. The results show that the solid, at 2 h of contact, can catalyze the degradation of 29%, improving its degradation capacity up to 60% when the process is assisted by UV irradiation, 65% when assisted by electric current, and 90% when assisted by UV irradiation and electric current. The maximum degradation was reached with the photoelectrocatalysis process at 6 h with a degradation of 95% and a half-life of 0.36 h. The efficiency of the catalytic process assisted by irradiation and electric

current with a Cu electrode is because the Cu^{2+} ions and with the photogenerated electrons decrease the speed of recombination of the electron–hole in the catalyst, and this generates a greater catalytic activity in the degradation of the Congo red dye. The degradation of the dye is favored by the presence of double bonds in the diazo groups (-N=N-) of the Congo red dye that become the preferred site for the attack of the OH radicals—the proximal or distal nitrogen atom of the azo group that leads to a variety of cleavage pathways resulting in several intermediary products that are completely degraded. At the conclusion of the degradation process, it is observed that the hydrotalcite is completely reconstructed with a high purity of crystalline phases, which can be used for further studies in the degradation of the azo type dye.

Supplementary Materials: The following are available online at https://www.mdpi.com/2073-4344/11/2/211/s1. Figure S1. (a) Linear correlation of the calibration curve by high-performance liquid chromatography (HPLC) of the industrial-grade synthetic dye Congo red and (b) solution of the calibration curve. Figure S2. Chromatograms of the liquid chromatography–mass spectrometry (LC–MS) analysis of Congo red after degradation: (a) Congo red standard, (b) catalyst, (c) photocatalyst, (d) electrocatalyst, (e) photoelectrocatalyst, and (f) possible degradation products of Congo red in the presence of hydrotalcites. Figure S3. (a) Solutions of dye at different concentrations for degradation, (b) solutions after degradation by the process of photocatalysis, and (c) solutions after degradation by photoelectrocatalysis. Figure S4. Diagram of the photoelectrocatalysis process.

Author Contributions: Conceptualization, E.R.-R., N.G.-O. and R.F.-R.; methodology, E.R.-R. and N.G.-O.; software R.F.-R. and S.A.-F., G.C.-J.; formal analysis, E.R.-R., N.G.-O., R.F.-R. and S.A.-F.; investigation, R.F.-R. and S.A.-F.; resources, E.R.-R. and G.C.-J.; data curation, S.A.-F. and G.C.-J.; writing—original draft preparation, E.R.-R. and R.F.-R.; writing—review and editing, N.G.-O.; E.R.-R.; funding acquisition, E.R.-R. and N.G.-O. All authors have read and agreed to the published version of the manuscript.

Funding: This research received no external funding. Funding was received from the resources of the University of Guanajuato.

Institutional Review Board Statement: Not applicable.

Informed Consent Statement: Not applicable.

Data Availability Statement: Not applicable.

Acknowledgments: We would like to especially thank the Directorate for Research and Postgraduate Support (DAIP) at the University of Guanajuato for their support in developing this project. We also thank the University of Guanajuato-CONACyT National Laboratories (National Laboratory for Characterization of Physicochemical Properties and Molecular Structure UG-UAA-CONACyT and Laboratory for Research and Technological Development in Advanced Coatings UG-CINVESTAV-IPN-CONACyT). Additionally, we thank the CONACyT for the graduate scholarship and the financing of the infrastructure project 255270.

Conflicts of Interest: The authors declare no conflict of interest.

References

1. Robinson, T.; McMullan, G.; Marchant, R.; Nigam, P. Remediation of dyes in textile effluent: A critical review on current treatment technologies with a proposed alternative. *Bioresour. Technol.* **2001**, *77*, 247–255. [CrossRef]
2. El Gaini, L.; Lakraimi, M.; Sebbar, E.; Meghea, A.; Bakasse, M. Removal of indigo carmine dye from water to Mg–Al–CO_3-calcined layered double hydroxides. *J. Hazard. Mater.* **2009**, *161*, 627–632. [CrossRef]
3. Chen, F.; Wu, X.; Bu, R.; Yang, F. Co–Fe hydrotalcites for efficient removal of dye pollutants via synergistic adsorption and degradation. *RSC Adv.* **2017**, *7*, 41945–41954. [CrossRef]
4. Van Der Zee, F.P.; Font, J.; Fortuny, A.; Fabregat, A. Towards advanced aqueous dye removal processes: A short review on the versatile role of activated carbon. *J. Environ. Manag.* **2012**, *102*, 148–160.
5. Guzmán-Vargas, A.; Limb, E.; Uriostegui-Ortega, G.A.; Oliver-Tolentino, M.A.; Rodríguez, E.E. Adsorption and subsequent partial photodegradation of methyl violet 2B on Cu/Al layered double hydroxides. *Appl. Surf. Sci.* **2016**, *363*, 372–380. [CrossRef]
6. Bilińska, L.; Gmurek, M.; Ledakowicz, S. Comparison between industrial and simulated textile wastewater treatment by AOPs—Biodegradability, toxicity and cost assessment. *Chem. Eng. J.* **2016**, *306*, 550–559. [CrossRef]

7. Ersoz, G.; Napoleoni, A.; Atalay, S. Comparative study using chemical wetoxidation for removal of reactive black 5 in the presence of activated carbon. *J. Environ. Eng.* **2013**, *139*, 1462–1469. [CrossRef]
8. Li, X.L.; Zhang, J.; Jiang, Y.C.; Hu, M.C.; Li, S.N.; Zhai, Q.G. Highly efficient biodecolorization/degradation of Congo red and alizarin yellow R bychloroperoxidase from Caldariomyces fumago: Catalytic mechanism anddegradation pathway. *Ind. Eng. Chem. Res.* **2013**, *52*, 13572–13579. [CrossRef]
9. Wang, Y.S.; Shen, J.H.; Horng, J.J. Chromate enhanced visible light driven TiO_2 photocatalytic mechanism on acid orange 7 photodegradation. *J. Hazard. Mater.* **2014**, *274*, 420–427. [CrossRef] [PubMed]
10. Erdemoglu, S.; Aksu, S.K.; Sayilkan, F.; Izgi, B.; Asilturk, M.; Sayılkan, H.; Frimmel, F.; Gucer, S. Photocatalytic degradation of Congo red by hydrothermally synthesized nanocrystalline TiO_2 and identification of degradation products by LC–MS. *J. Hazard. Mater.* **2008**, *155*, 469–476. [CrossRef] [PubMed]
11. Starukh, G. Photocatalytically Enhanced Cationic Dye Removal with Zn-Al Layered Double Hydroxides. *Nanoscale Res. Lett.* **2017**, *12*, 391. [CrossRef]
12. Janczarek, M.; Kowalska, E. On the Origin of Enhanced Photocatalytic Activity of Copper-Modified Titania in the Oxidative Reaction Systems. *Catalysts* **2017**, *7*, 317. [CrossRef]
13. Dorian, A.H.H.; Sorrell, C.C. Sand supported mixed-phase TiO_2 photocatalysts for water decontamination applications. *Adv. Eng. Mater.* **2014**, *16*, 248–254.
14. Pattnaik, S.P.; Behera, A.; Acharya, R.; Parida, K. Green exfoliation of graphitic carbon nitride towards decolourization of Congo-Red under solar irradiation. *J. Environ. Chem. Eng.* **2019**, *7*, 103456. [CrossRef]
15. Kumru, B.; Antonietti, M. Colloidal properties of the metal-free semiconductor graphitic carbon nitride. *Adv. Colloid Interfac. Sci.* **2020**, *283*, 102229. [CrossRef] [PubMed]
16. Zhao, Z.; Sun, Y.; Dong, F. Graphitic carbon nitridebased nanocomposites: A review. *Nanoscale* **2015**, *7*, 15–37. [CrossRef]
17. Hieu-Nguyen, C.; Chun-Chieh, F.; Ruey-Shin, J. Degradation of methylene blue and methyl orange by palladium-doped TiO_2 photocatalysis for water reuse: Efficiency and degradation pathways. *J. Clean. Prod.* **2018**, *202*, 413–427. [CrossRef]
18. Chong, M.N.; Jin, B.; Chow, C.W.K.; Saint, C. Recent developments in photocatalytic water treatment technology: A review. *Water Res.* **2010**, *44*, 2997–3027. [CrossRef]
19. Kushwaha, H.S.; Vaish, R. Enhanced visible light photocatalytic activity of curcumin-sensitized perovskite $Bi_{0.5}Na_{0.5}TiO_3$ for rhodamine 6G degradation. *Int. J. Appl. Ceram. Technol.* **2016**, *13*, 333–339. [CrossRef]
20. Subhan, M.A.; Saha, P.C.; Uddin, N.; Sarker, P. Synthesis, structure, spectroscopy and photocatalytic studies of nano multimetal oxide $MgO{\cdot}Al_2O_3$ ·ZnO and $MgO{\cdot}Al_2O_3$ ·ZnO curcumin composite. *Int. J. NanoSci. NanoTechnol.* **2017**, *13*, 69–82.
21. Li, Y.; Cui, W.; Liu, L.; Zong, R.; Yao, W.; Liang, Y.; Zhu, Y. Removal of Cr(VI) by 3D TiO_2 -graphene hydrogel via adsorption enriched with photocatalytic reduction. *Appl. Catal. B Environ.* **2016**, *199*, 412–423. [CrossRef]
22. Arotiba, O.A.; Orimolade, B.O.; Koiki, B.A. Visible light–driven photoelectrocatalytic semiconductor heterojunction anodes for water treatment applications. *Curr. Opin. Electrochem.* **2020**, *22*, 25–34. [CrossRef]
23. Turolla, A.; Bestetti, M.; Antonelli, M. Optimization of heterogeneous photoelectrocatalysis on nanotubular TiO2 electrodes: Reactor configuration and kinetic modelling. *Chem. Eng. Sci.* **2018**, *182*, 171–179. [CrossRef]
24. Figueras, F. Base Catalysis in the Synthesis of Fine Chemicals. *Top. Catal.* **2004**, *29*, 189–196. [CrossRef]
25. Cavani, F.; Trifirò, F.; Vaccari, A. Hydrotalcite-type anionic clays: Preparation, properties and applications. *Catal. Today* **1991**, *11*, 173–302. [CrossRef]
26. Rives, V. *Layered Double Hydroxides: Present and Future*, 1st ed.; Nova Science Publishers, Inc.: New York, NY, USA, 2001; pp. 9–321.
27. Timar, Z.; Varga, G.; Murath, S. Synthesis, characterization and photocatalytic activity of crystalline Mn(II) Cr(III)-layered double hydroxide. *Catal. Today* **2017**, *284*, 195–201. [CrossRef]
28. Ballarin, B.; Mignani, A.; Scavetta, E.; Giorgetti, M.; Tonelli, D.; Boanini, E.; Mousty, C. Ruta de síntesis para hidróxidos dobles en capas de nanopartículas de oro soportadas como catalizadores eficaces en la electro oxidación del metanol. *Langmuir* **2012**, *28*, 15065–15074. [CrossRef] [PubMed]
29. Zhang, H.; Chen, H.; Azat, S.; Mansurov, Z.; Liu, X.; Wang, J.; Su, X.; Wu, R. Super adsorption capability of rhombic dodecahedral Ca-Al layered double oxides for Congo red removal. *J. Alloy. Comp.* **2018**, *768*, 572–581. [CrossRef]
30. Ramos-Ramírez, E.; Tzompantzi-Morales, F.; Gutiérrez-Ortega, N.; Mojica-Calvillo, H.G.; Castillo-Rodríguez, J. Photocatalytic Degradation of 2,4,6-Trichlorophenol by MgO–$MgFe_2O_4$ Derived from Layered Double Hydroxide Structures. *Catalysts* **2019**, *9*, 454. [CrossRef]
31. Ramos-Ramírez, E.; Gutiérrez-Ortega, N.L.; Tzompantzi-Morales, F.; Barrera-Rodríguez, A.; Castillo-Rodríguez, J.C.; Tzompantzi-Flores, C.; Guevara-Hornedo, M.P. Photocatalytic Degradation of 2,4-Dichlorophenol on NiAl-Mixed Oxides Derivatives of Activated Layered Double Hydroxides. *Top. Catal.* **2020**, *63*, 546–563. [CrossRef]
32. Jawad, A.; Peng, L.; Liao, Z.; Zhou, Z.; Shahzad, A.; Ifthikar, J.; Chen, Z. Selective removal of heavy metals by hydrotalcites as adsorbents in diverse wastewater: Different intercalated anions with different mechanisms. *J. Clean. Prod.* **2018**, *211*, 1112–1126. [CrossRef]
33. Setshedi, K.; Ren, J.; Aoyi, O.; Onyango, M.S. Removal of Pb(II) from aqueous solution using hydrotalcite-like nanostructured material. *Int. J. Phys. Sci.* **2012**, *7*, 63–72.
34. Dias, A.C.; Fontes, M.P.F. Arsenic (V) removal from water using hydrotalcites as adsorbents: A critical review. *Appl. Clay. Sci.* **2020**, *191*, 105615. [CrossRef]

35. Nong, L.; Xiao, C.; Jiang, W. Azo dye removal from aqueous solution by organic-inorganic hybrid dodecanoic acid modified layered Mg-Al hydrotalcite. *Korean J. Chem. Eng.* **2011**, *28*, 933–938. [CrossRef]
36. Mustapha, M.; Derriche, Z.; Denoyel, R.; Prevot, V.; Forano, C. Thermodynamical and structural insights of orange II adsorption by $MgRAlNO_3$ layered double hydroxides. *J. Solid State Chem.* **2011**, *184*, 1016–1024. [CrossRef]
37. Sels, B.F.; de Vos, D.E.; Jacobs, P.A. Hydrotalcite-like anionic clays in catalytic organic reactions. *Catal. Rev.* **2001**, *43*, 443–488. [CrossRef]
38. Shakeel, M.; Arif, M.; Yasin, G.; Li, B.; Khan, H.D. Layered by Layered Ni-Mn-LDH/g-C3N4 Nanohybrid for Multi-Purpose Photo/electrocatalysis: Morphology Controlled Strategy for Effective Charge Carriers Separation. *Appl. Catal. B* **2018**, *242*, 485–498. [CrossRef]
39. Chen, X.; Yang, Z.; Wang, L.; Qin, H.; Tong, M. Synthesis of Hollow Spherical Zinc-Aluminum Hydrotalcite and Its Application as Zinc Anode Material. *J. Electrochem. Soc.* **2019**, *166*, A2589–A2596. [CrossRef]
40. Pan, L.; Huang, H.; Niederberger, M. Layered cobalt hydrotalcite as an advanced lithium-ion anode material with high capacity and rate capability. *J. Mater. Chem. A* **2019**, *7*, 21264–21269. [CrossRef]
41. Zhou, F.; Pan, N.; Chen, H.; Xu, X.; Wang, C.; Du, Y.; Li, L. Hydrogen production through steam reforming of toluene over Ce, Zr or Fe promoted Ni-Mg-Al hydrotalcite-derived catalysts at low temperature. *Energy Convers. Manag.* **2019**, *196*, 677–687. [CrossRef]
42. Garcia-Segura, S.; Brillas, E. Applied photoelectrocatalysis on the degradation of organicpollutants in wastewaters. *J. PhotoChem. Photobiol. C* **2017**, *31*, 1–35. [CrossRef]
43. Zhang, Y.; Cui, W.; An, W.; Liu, L.; Liang, Y.; Zhu, Y. Combination of photoelectrocatalysis and adsorption for removal of bisphenol A over TiO_2-graphene hydrogel with 3D network structure. *Appl. Catal. B* **2018**, *221*, 36–46. [CrossRef]
44. Ghenaatgar, A.; Tehrani, R.M.A.; Khadir, A. Photocatalytic degradation and mineralization of dexamethasone using WO3 and ZrO2 nanoparticles: Optimization of operational parameters and kinetic studies. *J. Water Process Eng.* **2019**, *32*, 100969. [CrossRef]
45. Tavakoli-Azar, T.; Reza-Mahjoub, A.; Seyed-Sadjadi, M.; Farhadyar, N.; Hossaini-Sadr, M. Improving the photocatalytic performance of a perovskite ZnTiO3 through ZnTiO3@S nanocomposites for degradation of Crystal violet and Rhodamine B pollutants under sunlight. *Inorg. Chem. Commun.* **2020**, *119*, 108091. [CrossRef]
46. Kamarudin, N.S.; Jusoh, R.; Jalil, A.A.; Setiabudi, H.D.; Sukora, N.F. Synthesis of silver nanoparticles in green binarysolvent for degradation of 2,4-D herbicide:Optimization and kinetic studies Faculty. *Chem. Eng. Res. Des.* **2020**, *159*, 300–314. [CrossRef]
47. Zhang, S.; Lin, T.; Chen, W.; Xu, H.; Tao, H. Degradation kinetics, byproducts formation and estimated toxicity of metronidazole (MNZ) during chlor(am)ination. *Chemosphere* **2019**, *235*, 21–31. [CrossRef]
48. Tantawi, O.; Baalbaki, A.; El Asmar, R.; Ghauch, A. A rapid and economical method for the quantification of hydrogen peroxide (H2O2) using a modified HPLC apparatus. *Sci. Total Environ.* **2019**, *654*, 107–117. [CrossRef]
49. Pinkernell, U.; Effkemann, S.; Karst, U. Simultaneous HPLC Determination of Peroxyacetic Acid and Hydrogen Peroxide. *Anal. Chem.* **1997**, *69*, 3623–3627. [CrossRef] [PubMed]
50. Huang, Y.; Wang, L.; Chen, B.; Zhang, Q.; Zhu, R. Detecting hydrogen peroxide reliably in water by ion chromatography: A method evaluation update and comparison in the presence of interfering components. *Environ. Sci. Water Res. Technol.* **2020**, *6*, 2396–2404. [CrossRef]
51. Nakata, K.; Fujishima, A. TiO_2 photocatalysis: Design and applications. *J. Photochem. Photobiol. C* **2012**, *13*, 169–189. [CrossRef]
52. Li, F.; Zhao, Y.; Liu, Y.; Hao, Y.; Liu, R.; Zhao, D. Solution combustion synthesis and visible light-induced photocatalytic activity of mixed amorphous and crystalline $MgAl_2O_4$ nanopowders. *Chem. Eng. J.* **2011**, *173*, 750–759. [CrossRef]
53. Sánchez-Cantú, M.; Galicia-Aguilar, J.A.; Santamaría-Juárez, D.; Hernández-Moreno, L.E. Evaluation of the mixed oxides produced from hydrotalcite-like compound's thermal treatment in arsenic uptake. *Appl. Clay. Sci.* **2016**, *121–122*, 146–153.
54. Nassar, M.Y.; Ahmed, I.S.; Samir, I. A novel synthetic route for magnesium aluminate ($MgAl_2O_4$) nanoparticles using sol–gel auto combustion method and their photocatalytic properties. *Spectrochim. Acta A* **2014**, *131*, 329–334. [CrossRef]
55. Bard, A.J.; Parsons, R.; Jordan, J. *Standard Potentials in Aqueous Solutions*; Marcel Dekker: New York, NY, USA, 1985.
56. Araña, J.; Peña Alonso, A.; Doña Rodríguez, J.M.; Herrera Melián, J.A.; González Díaz, O.; Pérez Peña, J. Comparative study of MTBE photocatalytic degradation with TiO2 and Cu-TiO_2. *Appl. Catal. B* **2008**, *78*, 355–363. [CrossRef]
57. Irie, H.; Kamiya, K.; Shibanuma, T.; Miura, S.; Tryk, D.A.; Yokoyama, T.; Hashimoto, K. Visible light-sensitive Cu(II)-grafted TiO_2 photocatalysts: Activities and X-ray absorption fine structure analyses. *J. Phys. Chem. C* **2009**, *113*, 10761–10766. [CrossRef]
58. Jalife-Jacobo, H.; Feria-Reyes, R.; Serrano-Torres, O.; Gutiérrez-Granados, S.; Peralta-Hernández, J.M. Diazo dye Congo red degradation using a Boron-doped diamond anode: An experimental study on the effect of supporting electrolytes. *J. Hazard. Mater.* **2016**, *319*, 78–83. [CrossRef] [PubMed]
59. Thomas, M.; Naikoo, G.A.; Sheikh, M.U.D.; Bano, M.; Khan, F. Effective photocatalytic degradation of Congo red dye using alginate/carboxymethyl cellulose/TiO_2 nanocomposite hydrogel under direct sunlight irradiation. *J. Photochem. Photobiol. A* **2016**, *327*, 33–43. [CrossRef]
60. Bhagwat, U.O.; Wu, J.J.; Asiri, A.M.; Anandan, S. Sonochemical Synthesis of Mg-TiO_2 nanoparticles for persistent Congo red dye degradation. *J. PhotoChem. Photobiol. A* **2017**, *346*, 559–569. [CrossRef]

61. Ullah, I.; Haider, A.; Khalid, N.; Ali, S.; Ahmed, S.; Khan, Y.; Ahmed, N.; Zubair, M. Tuning the band gap of TiO_2 by tungsten doping for efficient UV and visible photodegradation of Congo red dye. *Spectrochim. Acta A* **2018**, *204*, 150–157. [CrossRef]
62. Curkovic, L.; Ljubas, D.; Juretic, H. Photocatalytic decolorization kinetics of diazo dye Congo red aqueous solution by UV/TiO_2 nanoparticles. *React. Kinet. Mech. Catal.* **2010**, *99*, 201–208.